nature communications

Article

https://doi.org/10.1038/s41467-025-59000-0

Nitrogen deposition favors later leaf senescence in woody species

Received: 28 July 2024

Accepted: 8 April 2025

Published online: 17 April 2025

Check for updates

Jian Wang[1,2,5], Xiaoyue Wang[1,2,5], Josep Peñuelas[3,4], Hao Hua[1,2] & Chaoyang Wu[1,2]

China has experienced an unprecedented increase in nitrogen deposition over recent decades, threatening ecosystem structure, functioning, and resilience. However, the impact of elevated nitrogen deposition on the date of foliar senescence remains widely unexplored. Using 22,780 in situ observations and long-term satellite-based date of foliar senescence measures for woody species across China, we find that increased nitrogen deposition generally delays date of foliar senescence, with strong causal evidence observed at site-to-region scales. Changes in climate conditions and nitrogen deposition levels jointly controlled the direction of date of foliar senescence trends (advance or delay). The spatial variability of nitrogen deposition effects can be related to plant traits (e.g., nitrogen resorption and use efficiencies), climatic conditions, and soil properties. Moreover, elevated nitrogen deposition delays date of foliar senescence by promoting foliar expansion and enhancing plant productivity during the growing season, while its influence on evapotranspiration may either accelerate or delay date of foliar senescence depending on local water availability. This study highlights the critical role of nitrogen deposition in regulating date of foliar senescence trends, revealing a key uncertainty in modeling date of foliar senescence driven solely by climate change and its far-reaching implications for ecosystem-climate feedbacks.

In recent decades, China has witnessed an unprecedented surge in nitrogen (N) deposition ($N_{deposition}$), primarily due to anthropogenic activities like agricultural fertilization and industrial and automotive combustion[1–3]. Elevated $N_{deposition}$ could induce a nutrient imbalance by suppressing other essential nutrients like phosphorus, accelerate biodiversity loss, and impair soil health and fertility, cumulatively influencing ecosystem carbon (C) cycling and resilience[4–7]. Increased N availability prompts plants to remobilize nutrients across different tissues to optimize growth and metabolic processes, as N is a key component of proteins, nucleic acids, and other essential molecules involved in plant development[8–10]. One major consequence of nutrient remobilization is initiating the process of foliar senescence[11], however, the degree to which variations in $N_{deposition}$ influence date of foliar senescence (DFS) trends may vary across space and time[12,13], necessitating a thorough comprehension of $N_{deposition}$-DFS relationship.

Plant autumn phenology, particularly DFS, plays a critical role in regulating the length of the growing season and influencing nutrient and C cycles in ecosystems[14–17]. As such, DFS has been widely incorporated into ecosystem models to reconstruct historical C uptake patterns and predict future variations[17,18]. The gradually shortening photoperiod during autumn has been considered the primary trigger for DFS, enabling trees to reallocate nutrients from leaves before frost damage occurs[19,20]. Additionally, rising temperature, increased precipitation, and reduced wind speed have been shown to contribute to

[1]The Key Laboratory of Land Surface Pattern and Simulation, Institute of Geographical Sciences and Natural Resources Research, Chinese Academy of Sciences, Beijing 100101, China. [2]University of the Chinese Academy of Sciences, Beijing 100049, China. [3]CSIC, Global Ecology Unit CREAF-CSIC-UAB, Bellaterra, Barcelona 08193 Catalonia, Spain. [4]CREAF, Cerdanyola del Valles, Barcelona 08193 Catalonia, Spain. [5]These authors contributed equally: Jian Wang, Xiaoyue Wang. e-mail: wucy@igsnrr.ac.cn

delayed DFS to varying extents[21–23]. Although studies have also highlighted the regulatory effects of $N_{deposition}$ on DFS trends, findings remain inconsistent[24–27]. In N-poor habitats, increased $N_{deposition}$ can alleviate nutrient limitations, sustain photosynthetic capacity, and slow chlorophyll degradation, thereby delaying DFS[12,24]. However, the impact of $N_{deposition}$ on DFS varies across species due to differences in species-specific N resorption efficiency, growth strategies, and environmental conditions[28,29]. In some cases, excessive $N_{deposition}$ may disrupt plant nutrient absorption, leading to "luxury consumption" of N and reduced N use efficiency[6]. These nutrient imbalances and metabolic disruptions can potentially accelerate DFS, as plants prioritize survival by reallocating resources from older leaves[30]. In addition to nutrient availability and limitation, elevated $N_{deposition}$ may influence DFS indirectly through biophysical processes, such as regulation of foliar area[24], evapotranspiration[22], and C sink capacity[31]. Most previous studies have relied on short-term fertilization experiments focusing on one or a few species, creating substantial uncertainty in assessing $N_{deposition}$ effects on DFS. This highlights the need for a comprehensive, multi-scale investigation into how $N_{deposition}$ influences DFS in natural ecosystems.

In this work, by analyzing in situ observations across 380 woody species, encompassing 22,780 site-year DFS records, along with satellite-based DFS estimates from Global Inventory Modeling and Mapping Studies (GIMMS, 1982–2020) and Moderate Resolution Imaging Spectroradiometer (MODIS, 2001–2020) (Supplementary Fig. 1, Table 1), we show that elevated $N_{deposition}$ tends to delay DFS across site-to-region scales for woody species in China. The spatial variability of $N_{deposition}$ effects is likely driven by differences in plant N resorption and use efficiency. Finally, we establish potential linkages between $N_{deposition}$ and DFS through foliar development, photosynthesis and evapotranspiration processes.

Results

Responses of DFS trends to $N_{deposition}$ variations

To uncover causal relationships in the time series data of $N_{deposition}$ and DFS, we used a causal structure learning method, i.e., Peter–Clark Momentary Conditional Independence Plus (PCMCI+), to address issues like temporal autocorrelation, indirect links and effects of climatic drivers (Methods, Fig. 1a, b). We identified directional causality from $N_{deposition}$ to DFS in 77.3, 71.9, and 63.6% of the time series for

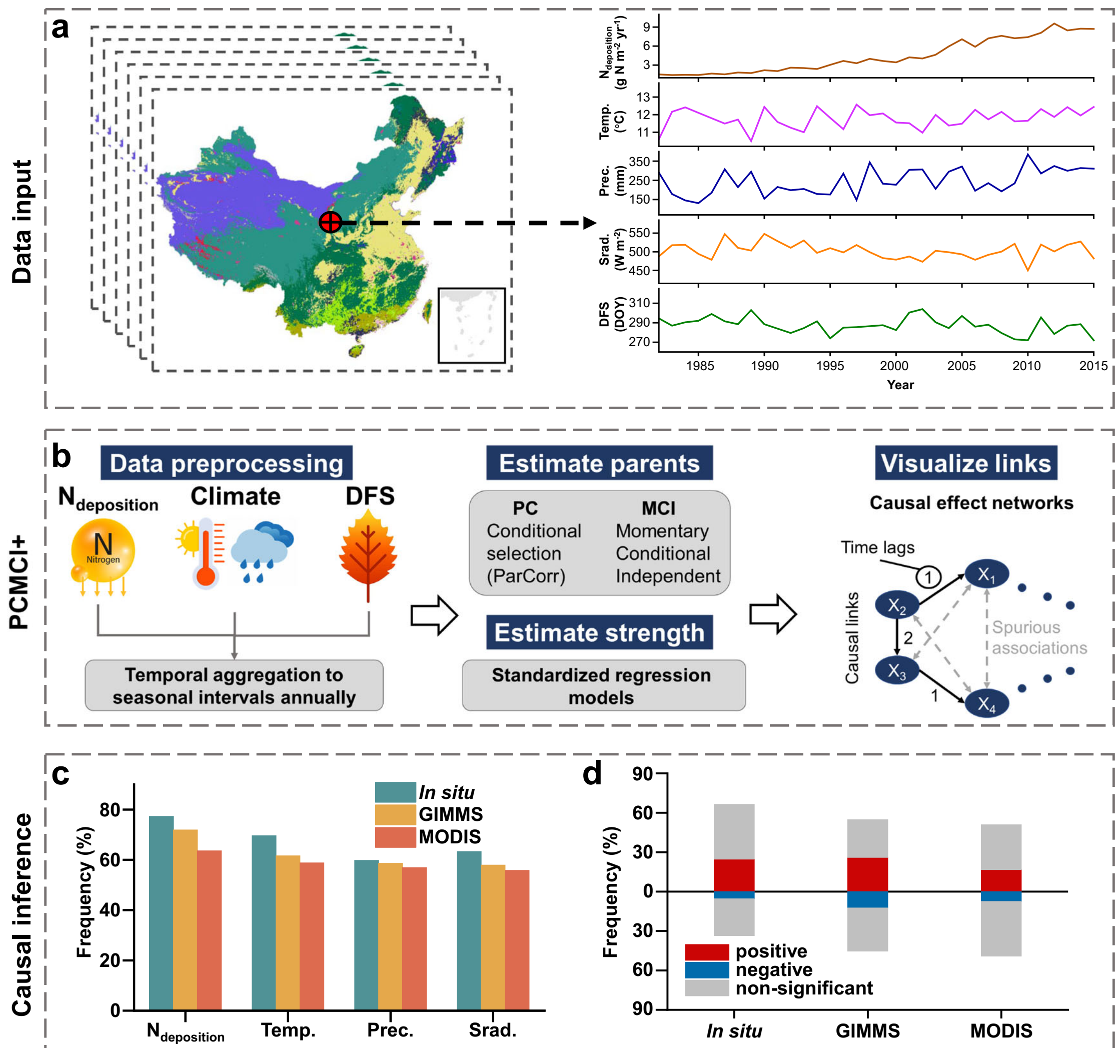

Fig. 1 | Causality and correlation between nitrogen deposition ($N_{deposition}$) and date of foliar senescence (DFS) at site and regional scales. a, b The framework of casual analysis using the PCMCI+ method (Methods). Data input includes site-species-specific or pixel-level time series of $N_{deposition}$, temperature (Temp.), precipitation (Prec.), shortwave radiation (Srad.), and DFS. **c** The frequencies of the time series with causality from climatic drivers and $N_{deposition}$ to DFS for in situ, GIMMS, and MODIS-based analyses. **d** The distribution of the time series with significantly positive, significantly negative, and non-significant partial correlations between $N_{deposition}$ and DFS, after excluding the effects of climate change. Significance was set at $p < 0.05$. A two-sided t-test was used to assess the significance of the partial correlation analysis. Source data are provided as a Source Data file.

in situ (site-species-specific), GIMMS, and MODIS (pixel-level) analyses, respectively, which are comparable with climatic drivers, i.e., temperature, precipitation, and shortwave radiation (Fig. 1c). For in situ-based analysis, 66.5% (24.7%, $p < 0.05$) of the DFS time series exhibited positive partial correlations with $N_{deposition}$, while only 33.5% (5.4%, $p < 0.05$) showed negative partial correlations. Satellite-based DFS analyses yielded similar results: 54.7% (26.1%, $p < 0.05$) and 51.3% (16.7%, $p < 0.05$) of pixels demonstrated positive correlations, while 45.3% (12.4%, $p < 0.05$) and 48.7% (7.4%, $p < 0.05$) exhibited negative correlations for GIMMS and MODIS, respectively (Fig. 1d). Grouping vegetation into forest and shrub generates similar results at site-to-region scales (Supplementary Fig. 2). Field measurements of $N_{deposition}$, including wet and dry deposition (NHx and NOy), also showed positive correlations with DFS, further confirming the delaying effects of $N_{deposition}$ on DFS (Supplementary Fig. 3).

We further assessed the spatial consistency between directions of DFS trends (advance or delay) and actual effects of each driver. For each time series, the actual effects of each driver were determined based on the sign of the product between the driver's trend and the partial correlation coefficient with DFS, where a positive sign indicates delay and a negative sign indicates advance (Methods). Our analysis found that 82% of the site-species-specific time series exhibited spatial consistency between the directions of DFS trends and the actual effect of $N_{deposition}$, while only 52%, 52%, and 50% of the time series showed spatial consistency for temperature, precipitation, and shortwave radiation, respectively (Fig. 2a). Similar patterns were observed in the GIMMS and MODIS analyses (Fig. 2b, c), with only minor variations in these proportions. Additionally, GIMMS and MODIS analyses showed comparable spatial consistency, with 68.3% of areas displaying consistently matched directions for $N_{deposition}$ (Fig. 2d).

Spatial attribution analysis of $N_{deposition}$ effects

We ranked the relative importance of various biotic and abiotic factors in explaining the spatial variability of $N_{deposition}$ effects, here $N_{deposition}$ effects were determined as the partial correlation coefficients between $N_{deposition}$ and DFS, using a random forest model with the Shapley Additive Explanations (SHAP) analysis (Methods). Among all factors, plant N resorption and use efficiency, along with climate conditions (i.e., multi-year mean shortwave radiation and temperature), were the most influential, together accounting for the spatial variability of $N_{deposition}$ effects in forest plants (Fig. 3a, Supplementary Fig. 4a). Grouping all factors into four catergories indicates that N-related factors were more important than climate, vegetation, and soil factors. Additionally, the SHAP values of the random forest model revealed that areas with higher N resorption efficiency or lower N use efficiency often exhibited a positive correlation between DFS and $N_{deposition}$, as confirmed by the variations in SHAP values along plant N resorption and use efficiency (Fig. 3b, c, Supplementary Fig. 4b, d). Notably, areas with better plant conditions, indicated by higher above-ground biomass, vegetation optical depth (a proxy of canopy biomass and water content), species richness, and forest age, tended to show negative correlations between DFS and $N_{deposition}$ (Fig. 3a). Similar patterns were observed for shrub plants, where N availability, temperature, and N resorption efficiency predominantly explained the spatial variability of $N_{deposition}$-DFS correlations (Supplementary Figs. 5 and 6).

Potential mediating processes underlying $N_{deposition}$-DFS relationship

We tested three hypotheses to explain the temporal linkage between $N_{deposition}$ and DFS: (H1) elevated $N_{deposition}$ expands foliar area and slows chlorophyll degradation during the growing season, thereby delaying DFS[12,24]; (H2) if the growing season's duration is constrained by the C sink capacity of trees, increased productivity due to $N_{deposition}$ should lead to earlier DFS[31]; and (H3) $N_{deposition}$ could increase evapotranspiration (ET) rates and accelerate soil and plant water loss, resulting in earlier DFS[22].

To test these hypotheses, we performed partial correlation analyses and structural equation modeling (SEM) using three mediators during the growing season: leaf area index (LAI), solar-induced chlorophyll fluorescence (SIF, a satellite-based proxy for photosynthesis), and ET (Methods). All three mediators exhibited predominantly positive partial correlations with $N_{deposition}$, suggesting that $N_{deposition}$ stimulates plant growth and productivity and associated water loss during the growing season (Fig. 4a). An increase in LAI was associated with delayed DFS, as indicated by predominantly positive correlations (16.5% positive vs. 8.2% negative; $p < 0.05$). Increased SIF during the growing season showed positive correlations with DFS in 20.1% of the areas, nearly twice the percentage of regions with negative correlations (10.9%) ($p < 0.05$). ET exhibited divergent effects on DFS with no dominant pattern (11.3% positive vs. 10.6% negative; $p < 0.05$) (Fig. 4b), and positive ET effects were found in regions with relatively high soil moisture (Supplementary Fig. 7).

We further categorized regions into two groups based on the correlation between $N_{deposition}$ and DFS: (G1) pixels with significantly positive correlations, and (G2) pixels with significantly negative correlations ($p < 0.05$). Separate SEM analyses for the two groups revealed distinct pathway effects. Elevated $N_{deposition}$ increased LAI, SIF, and ET in both groups. In regions with positive correlations (G1), three potential mediators contributed to a delay in DFS to varying extents (Fig. 4c). Conversely, in regions with negative correlations (G2), increased LAI marginally delayed DFS, but higher SIF and ET were associated with earlier DFS, collectively leading to earlier DFS (Fig. 4d). In situ- and MODIS-based analyses generated similar results (Supplementary Figs. 8 and 9), confirming that $N_{deposition}$-driven foliar expansion, increased productivity, and accelerated ET during the growing season collectively and variably influence DFS trends. Overall, these findings support hypothesis H1, while refuting H2 and H3. Because the cumulative productivity during the growing season predominantly exhibited delaying effects on DFS, with no consistent delaying or advancing effects of ET on DFS.

Discussion

Understanding the ecological consequences of elevated $N_{deposition}$ is pivotal for unraveling the complex interplay between vegetation and climate, which are essential for projecting future C cycles in terrestrial ecosystems[4]. As a key determinant of Rubisco and chlorophyll synthesis, plant leaf N that affected by $N_{deposition}$ rates could influence photosynthetic capacity, chloroplast degradation, and foliar senescence accordingly[25,29]. Using in situ records and satellite-based measures of DFS for woody species in China, we identified a notable delaying effect of $N_{deposition}$ on DFS, consistent with findings from previous N addition experiments[12,24]. The prevalence of the delaying effect was more pronounced at the site scale (in situ) than at the regional scale (e.g., GIMMS and MODIS), likely due to pixel mixing effects caused by coarse spatial resolutions (Fig. 1c). Causal analyses incorporating temporal variations of climatic factors and $N_{deposition}$ confirmed the notable influence of $N_{deposition}$ on DFS variations for woody species, which could be comparable to, or even stronger than, the effects of climate change (Fig. 1c).

High spatial variability in $N_{deposition}$ effects indicates non-uniform responses of DFS, likely mediated by local plant traits, climatic conditions, and soil properties[27]. For example, plants with high N resorption efficiency or low N use efficiency, particularly in nutrient-poor environments, exhibited positive response of DFS to $N_{deposition}$ (Fig. 3, Supplementary Figs. 4–6). This response may reflect an ecologically important strategy for woody species to conserve, restore, and relocate nutrients for subsequent growth and fitness[32,33]. In N-limited regions, delayed DFS combined with high leaf N resorption efficiency

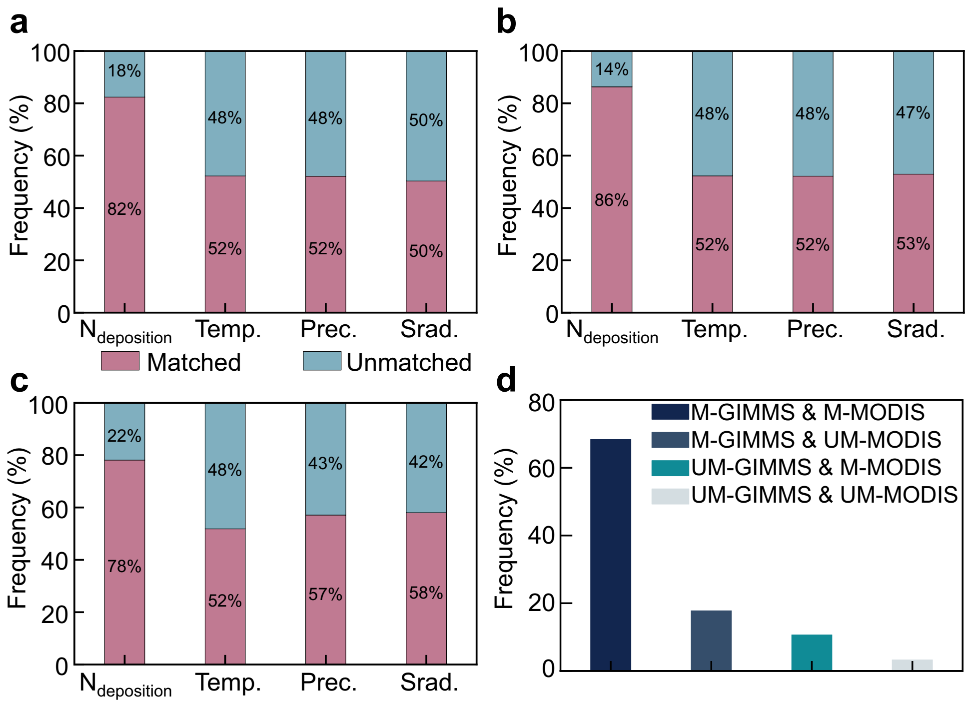

Fig. 2 | Spatial consistency between the direction of date of foliar senescence (DFS) trends and actual effects of drivers. a–c Frequencies of the time series with spatial consistency (matched) or inconsistency (unmatched) between the direction of DFS trends and actual effects of each driver, i.e., nitrogen deposition ($N_{deposition}$), temperature (Temp.), precipitation (Prec.), and shortwave radiation (Srad.), for in situ (site-species-specific) (**a**), GIMMS (**b**), and MODIS (pixel-level) (**c**) analyses (Methods). **d** Pixel-level comparison (GIMMS vs. MODIS) of spatial consistency between the directions of DFS trend and actual effects of $N_{deposition}$. M and UM refer to matched and unmatched, respectively. Source data are provided as a Source Data file.

helps plants to meet their N demands[24]. Additionally, the relationship between $N_{deposition}$ and DFS may be influenced by above-ground biomass, species richness, and forest age (Fig. 3a, Supplementary Fig. 4a), underscoring the importance of plant characteristics, species composition, and community assemblage in regulating $N_{deposition}$ effects. A recent study emphasized the role of $N_{deposition}$ in driving westward shifts of European forest plants, linked to recovery from past acidifying deposition[34], suggesting the interactive effects of $N_{deposition}$ and soil acid stress on vegetation dynamics. Similarly, we observed that $N_{deposition}$ tends to accelerate foliar senescence in low-pH regions, indicating a dependence of $N_{deposition}$ effects on soil pH conditions (Fig. 3a, Supplementary Fig. 10).

Exploring the temporal linkage between $N_{deposition}$ and DFS presents additional challenges. We tested three hypotheses regarding $N_{deposition}$-induced foliar expansion, productivity enhancement, and water loss. Our findings suggest that increases in LAI can slow chlorophyll degradation, thereby delaying DFS. While previous studies have suggested a negative relationship between growing-season productivity and DFS[29]—attributed to sink limitations in plants and the premise that the growing season's duration is constrained by the C sink capacity of trees—our results contrast with this view. Using SIF as a proxy for productivity, we identified a predominantly positive correlation between growing-season productivity and DFS (Fig. 4b), aligning with evidence from eddy-covariance flux measurements[35] and free-air CO_2 enrichment (FACE) experiments[36]. Currently, uncertainties remain regarding whether woody plants experience sink limitations under real-world conditions[37] and whether $N_{deposition}$ influences sink activity and capacity, particularly in N-limited regions[38]. Given these ongoing debates, future research should prioritize process- and mechanism-based investigations of the sink regulation of photosynthesis and productivity-DFS relationship, accounting for temporal dynamics and spatial scales. Additionally, while some studies have linked ET-induced water loss with accelerated DFS[22,30], our results suggest that this effect varies with regional water availability. Enhanced ET, driven by higher photosynthetic activity, may delay DFS in water-sufficient regions[39], whereas limited soil water availability can advance DFS due to ET-induced water stress (Supplementary Fig. 7). The intermediary roles of LAI, SIF, and ET provide a more nuanced understanding of the $N_{deposition}$-DFS relationship. Nonetheless, further studies, including N-control experiments measuring plant C/N metabolism, nutrient remobilization, abscisic acid accumulation, and chlorophyll degradation, are essential to elucidate the mechanisms underlying $N_{deposition}$-DFS relationship. Beyond this, excessive $N_{deposition}$ could lead to the limitation of other nutrients, particularly phosphorus. This shift from N-limited to phosphorus-limited conditions may impair plant growth and functions[6], further regulating the timing and speed of foliar senescence.

Given China's rapid industrialization and urbanization, elevated $N_{deposition}$ and its ecological consequences are likely to become major drivers of ecosystem dynamics[4,5]. Our findings underscore the regulatory role of $N_{deposition}$ in shaping divergent DFS trends and the underlying linkages for woody species, highlighting the importance of incorporating $N_{deposition}$ effects into existing phenological models that solely driven by climate change. This study provides valuable insights into the phenological regulation of vegetation feedbacks to the climate system under future $N_{deposition}$ scenarios.

Methods

In situ records of DFS

In this study, we compiled all available in situ records of DFS for woody species since the 1980s from the Chinese Phenological Observation Network (CPON)[40]. To identify and exclude potential outliers, we applied the median absolute deviation (MAD) method, which is less sensitive to outliers than the standard deviation. Specifically, the MAD

https://doi.org/10.1038/s41467-025-59000-0

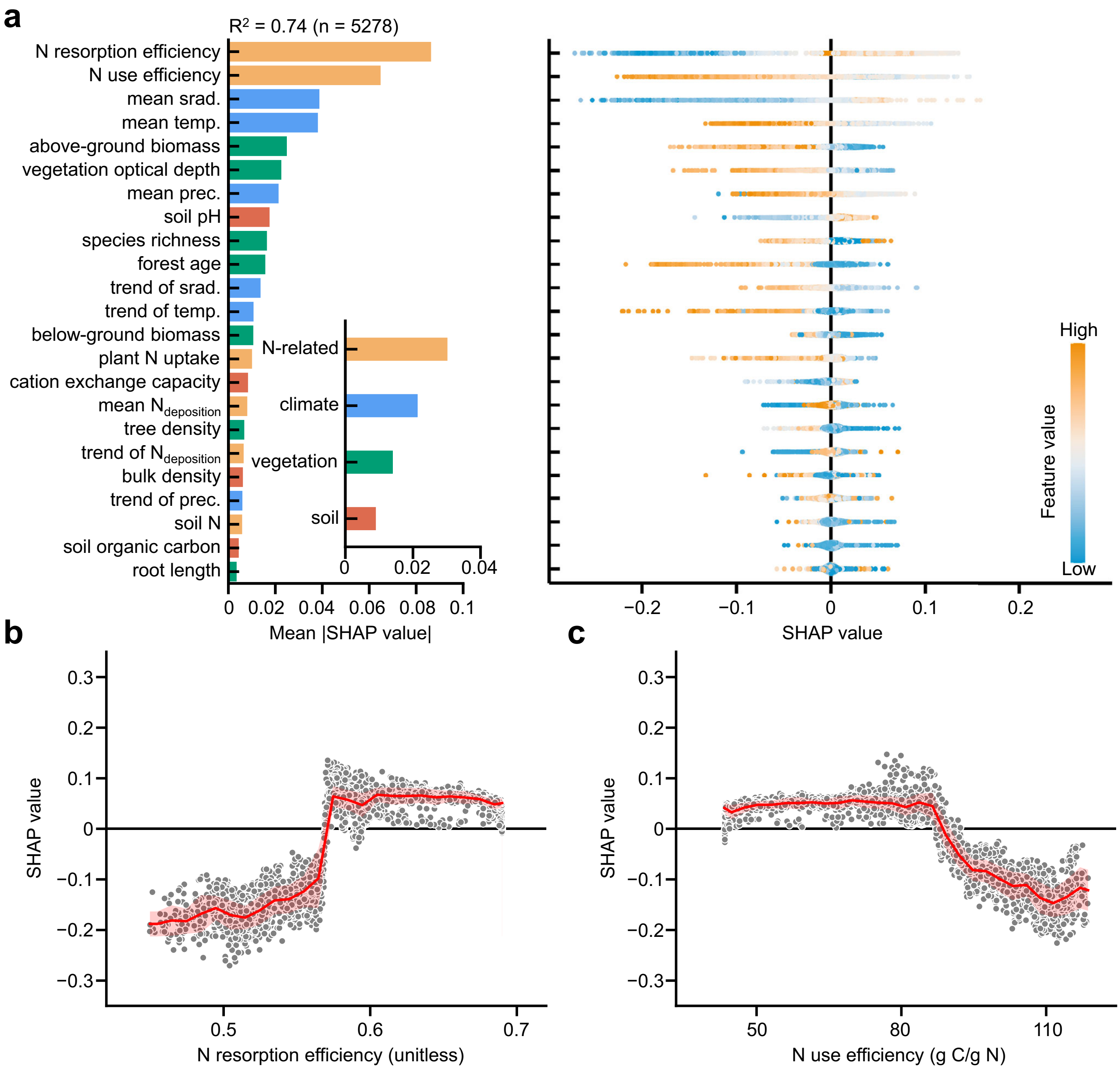

Fig. 3 | Spatial attribution of the relationship between nitrogen deposition ($N_{deposition}$) and date of foliar senescence (DFS) for forest plants. a The relative importance of biotic and abiotic factors controlling the spatial variability of $N_{deposition}$-DFS correlations, determined by a random forest model (R^2 = 0.74, n = 5278) using mean absolute SHAP values. The inner subplot indicates the averaged importance of N-related, climate, vegetation, and soil factors. The right beeswarm plot shows the distribution of SHAP values for each factor. **b**, **c** Variations of SHAP values along with plant N resorption efficiency (**b**) and N use efficiency (**c**). The lines and bands indicates the means and standard deviations, respectively. Source data are provided as a Source Data file.

for a site-species-specific DFS dataset (DFS_1, DFS_2,..., DFS_i) is calculated as:

$$\mathrm{MAD} = \mathrm{median}\left(\left|\mathrm{DFS}_i - \mathrm{median}(\mathrm{DFS})\right|\right) \quad (1)$$

For each species at a given site, any DFS record exceeding 2.5 times the MAD was considered an outlier[41]. To ensure robust analyses with sufficient observations, we excluded site-species-specific DFS time series with fewer than 10 years of data. This resulted in a total of 1400 time series from 46 sites and 380 woody species (including 211 forest and 169 shrub species) for the period 1982–2018. Detailed information on the distribution and descriptions of the in situ sites can be found in Supplementary Fig. 1 and Supplementary Data 1.

Satellite remote sensing-based measures of DFS

We used Normalized Difference Vegetation Index (NDVI) data derived from GIMMS 3 g+ (1982–2020, 1/12°) and MODIS (MOD13C2, 2001-2020, 0.05°) to determine satellite-based proxies for DFS. Both datasets have been widely employed to estimate DFS based on the seasonal dynamics of vegetation greenness[22,39]. To mitigate the influence of snow, NDVI values affected by snow were replaced with average NDVI values from snow-free periods during winter (December-February) over multiple years[42]. A modified Savitzky-Golay filter was applied to remove anomalous values and reconstruct the NDVI time series[43]. Regions with an average annual NDVI below 0.1 were excluded to eliminate areas with sparse vegetation. To reduce uncertainties associated with a single approach, we calculated DFS using two distinct

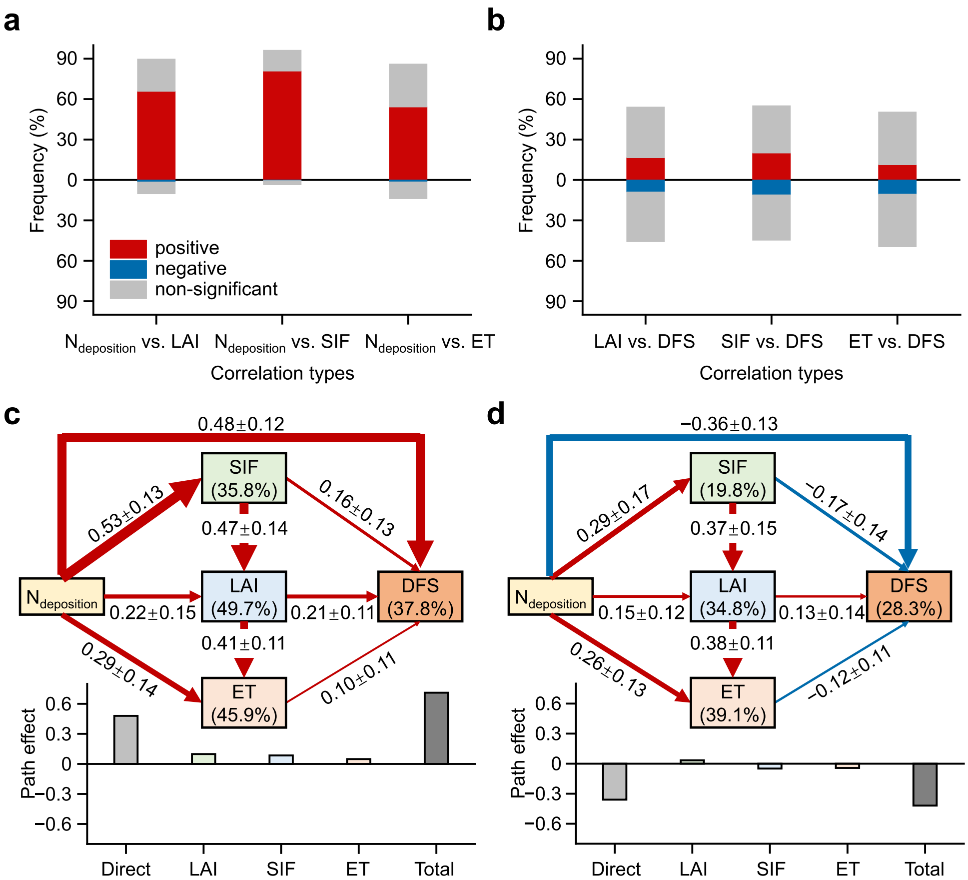

Fig. 4 | Temporal linkage between nitrogen deposition ($N_{deposition}$) and date of foliar senescence (DFS) driven by potential mediators. a, b The frequencies of pixels with significantly positive, significantly negative, and non-significant partial correlations between $N_{deposition}$ and mediators (**a**) and between mediators and DFS (**b**), after controlling the effects of temperature, precipitation, and shortwave radiation. Mediators include growing-season leaf area index (LAI), solar-induced chlorophyll fluorescence (SIF), and evapotranspiration (ET). Significance was set at $p < 0.05$. A two-sided t-test was used to assess the significance of the partial correlation analysis. **c, d** The SEMs describing the positive ($n = 5287$) (**c**) and negative ($n = 1598$) (**d**) relationships between $N_{deposition}$ and GIMMS-based DFS considering the effects of mediators. Percentages close to variables refer to the mean variance accounted for by the model (R^2). Numbers on the arrows indicate the mean and standard deviation of standardized path coefficients, respectively. Arrow widths reflect the magnitudes of the coefficients. The lower subplots show the direct, intermediary (LAI, SIF, and ET) and total effects of $N_{deposition}$ on DFS. Source data are provided as a Source Data file.

methods: the dynamic-threshold approach[44] and the double-logistic function[22].

For each pixel, we calculated annual NDVI ratios using the following formula:

$$NDVI_{ratio} = \frac{NDVI - NDVI_{min}}{NDVI_{max} - NDVI_{min}} \tag{2}$$

where NDVI represents the daily NDVI value, and $NDVI_{min}$ and $NDVI_{max}$ are the annual minimum and maximum NDVI values, respectively. The DFS was defined as the day of the year when the $NDVI_{ratio}$ declined to 0.5.

To segment the annual NDVI curve into two sections, we identified the peak NDVI value and applied a piecewise logistic function to fit each segment:

$$y(t) = a_1 + (a_2 - a_7 t)\left(\frac{1}{1 + e^{(a_3 - t)/a_4}} - \frac{1}{1 + e^{(a_5 - t)/a_6}}\right) \tag{3}$$

where t is time in days, $y(t)$ is the NDVI at time t. a_1 - a_7 are fitting parameters: background NDVI (a_1), the difference between the background and the late summer/autumn plateau amplitude (a_2), the midpoints for green-up (a_3) and senescence/abscission (a_5), transition curvature parameters (a_4 and a_6), and the summer green-down parameter (a_7). The DFS was identified as the local extrema in the rate of change within the second segment of the curve.

Note that satellite-based DFS estimates are derived from seasonal variations in vegetation greenness (i.e., NDVI), which may introduce biases when compared to in situ DFS measurements, particularly due to spatial scale mismatches and the pixel-mixing effects. To mitigate these biases, we conducted independent analyses for each dataset (in situ records and the two satellite-based DFS data) rather than directly integrating or comparing them[41].

$N_{deposition}$, climatic, and other ancillary data

We used an observation-based $N_{deposition}$ product originally spanning from 1982–2012[45]. More than 500 observational records of $N_{deposition}$ from 163 sites, along with county-level N fertilizer data and province-level energy consumption data across China, were utilized to enhance and generate the $N_{deposition}$ data. To extend the $N_{deposition}$ data to 2020, we applied an autoregressive integrated moving average (ARIMA) model, which is widely used to predict future values based solely on past observations, particularly for relatively small datasets. We first tested the stationarity of the $N_{deposition}$ data using the Augmented Dickey-Fuller (ADF) test. We then used data from 1982-2005 as the historical training set and data from 2006-2012 as the test set for each pixel. The overall relative RMSE was 7.3 ± 4.4%, demonstrating the applicability and reliability of ARIMA in predicting $N_{deposition}$. Finally, we applied the ARIMA model to estimate $N_{deposition}$ for 2013–2020. We also collected field measurements of $N_{deposition}$ data from published papers[46], with a total of 6934 site-year records. The field data includes wet deposition (NH4 and NO3) and dry deposition (NH3, NH4 + , NO2, NO3, and HNO3).

The monthly climatic data, including temperature, precipitation, and shortwave radiation, were obtained from CN05.1[47]. We used the mean temperature, total precipitation, and shortwave radiation from July to September to represent the climate drivers of DFS. A high-resolution China Land Cover Dataset (CLCD v1.1, 30 m)[48] was used to define the spatial extent of woody species, including forests and shrubs. To minimize the effects of land cover changes in our analyses, we identified and excluded all pixels with land cover changes from 1980 to 2020 using the CLCD product.

For the spatial analysis of the $N_{deposition}$-DFS relationship, we used multiple N-related and vegetation factors, including plant N resorption efficiency, plant N use efficiency, plant N uptake[49], above- and below-ground biomass[50], species richness[51], forest age[52], tree density[53], and maximum root length[54]. Additionally, several soil properties, including soil pH, cation exchange capacity, N content, and organic C, were sourced from the SoilGrid 2.0[55]. We determined depth-weighted (0–200 cm) average value for each soil property. The Ku-band vegetation optical depth was derived from a long-term microwave Vegetation Optical Depth Climate Archive (VODCA)[56]. For the temporal analyses, we used time series data of LAI[57], SIF[58], and ET[59] as mediators to link $N_{deposition}$ and DFS. Detailed information regarding data description, spatial and temporal resolution, temporal coverage, and data source of all datasets we used can be found in Supplementary Table 1.

Temporal trend analyses

We applied the Theil-Sen slope estimator to assess the temporal trends of DFS, $N_{deposition}$, and climatic factors at site-to-region scales. This slope estimator is a non-parametric method and ensures that the slope estimate is not unduly influenced by extreme data points, making it especially suitable for small datasets. Additionally, we evaluated the trends using the Mann-Kendall trend test at a significance level of 0.05[22,41]. We found predominantly delaying trends in *in-situ* DFS, with 29.5% of the time series showing delaying trends, while only 6.5% of the time series showing advancing trends (Supplementary Fig. 11). Satellite-based DFS showed more divergent patterns of temporal trends, with 34.5% (25.7%) and 11.1% (6.8%) of pixels showing delaying (advancing) trends for GIMMS (1982-2020) and MODIS (2001-2020), respectively (Supplementary Fig. 12a, b). We also compared the spatial consistency of DFS trends for GIMMS and MODIS for overlapped period (2001-2020), and found similar spatial patterns of DFS shifting directions (Supplementary Fig. 12c, d).

Analyses of the relationship between $N_{deposition}$ and DFS

To support the causal claim that changes in $N_{deposition}$ influence interannual variations in DFS, we employed a causal inference method known as PCMCI+ to determine the direction of causality. The PCMCI causal discovery framework integrates the PC algorithm (a causal discovery method based on conditional independence) with the Momentary Conditional Independence (MCI) test, designed to address the autocorrelation commonly present in time series data[60,61]. We used an extended version of this framework, PCMCI + , which can identify both lagged and contemporaneous causal links[62]. Time series data of DFS and potential drivers (i.e., $N_{deposition}$, temperature, precipitation, and shortwave radiation) obtained from gridded data served as inputs. Focusing on linear dependencies, we applied linear partial correlation as the conditional independence test (Fig. 1a, b). The PCMCI+ parameters were set as follows: the minimum time lag was set to 0 to capture contemporaneous relationships, and the maximum time lag was set to 5 to account for dependencies spanning up to 5 years between DFS and $N_{deposition}$. The significance level was set to 0.1 for all tests. The strength of causal links was measured by the MCI partial correlation value, and the identified cause-effect relationships were represented in causal graphs. The causal discovery methods used in this study are implemented in the Python package Tigramite, available at https://github.com/jakobrunge/tigramite. Overall, the PCMCI+ results indicated that $N_{deposition}$ influences DFS across site-to-region scales (Fig. 1c).

After establishing the causal relationship between $N_{deposition}$ and DFS, we conducted partial correlation analyses to investigate how DFS responds to changes in $N_{deposition}$ and climatic drivers. In calculating the partial correlation coefficients between DFS and each driver, the effects of other factors were controlled. We also applied partial correlation analysis to quantify the responses of DFS to field measurements of $N_{deposition}$ for each deposition type, including wet deposition (NH_4 and NO_3) and dry deposition (NH_3, NH_4^+, NO_2, NO_3, and HNO_3). For the spatial analysis, we compiled site-specific average $N_{deposition}$, temporal trends of DFS (from GIMMS), and climatic factors (temperature, precipitation, and shortwave radiation). We then calculated the partial correlation coefficient between $N_{deposition}$ and DFS trends, excluding the effects of climatic trends (Supplementary Fig. 3a). For the temporal analysis, we calculated the temporal anomalies of $N_{deposition}$, DFS, and climatic factors (at least 5 years) and pooled these anomalies to determine the partial correlation between $N_{deposition}$ and DFS, controlling the effects of climatic anomalies (Supplementary Fig. 3b).

For each driver, we also identified the direction of actual effect on DFS (DoAE, advance or delay) by analyzing the sign of the product of its temporal trend and the partial correlation coefficient between DFS and that driver for each time series.

$$\mathrm{DoAE}_d = \mathrm{Sign}\left(\mathrm{ParCor}_d \times \mathrm{Tr}_d\right) \tag{4}$$

where d represents a driver, ParCor and Tr denote the partial correlation coefficient between DFS and the driver, and the temporal trend of the driver, respectively. For each time series, a positive DoAE indicates a delay, and a negative DoAE represents an advance.

We then compared the spatial consistency between the direction of DFS and the DoAE for each driver. For each site-species-specific time series (in situ) or pixel (GIMMS and MODIS), if the DoAE of a driver aligns with the direction of DFS, we defined the actual effect of this factor as "matched"; otherwise, it was considered "unmatched" (Fig. 2). We also compared the agreements of matched and unmatched for GIMMS and MODIS results. To match the spatial resolution, MODIS data was resampled to 1/12° before analysis.

Spatial attribution analysis of $N_{deposition}$-DFS relationship

We utilized explainable machine learning with SHapley Additive exPlanations (SHAP) to identify the key drivers of the spatial distribution of $N_{deposition}$ effects. Various biotic and abiotic factors were grouped into four categories: (1) N-related factors, including $N_{deposition}$, plant N resorption efficiency, N use efficiency, and N uptake; (2) climate factors, including temperature, precipitation, and shortwave radiation; (3) vegetation factors, such as above- and below-ground biomass, Ku-band vegetation optical depth (a proxy of water content/biomass of the canopy), species richness, forest age, tree density, and root length; and (4) soil factors, including soil pH, cation exchange capacity, bulk density, and soil organic C. For multi-year $N_{deposition}$ and climate variables, both mean values and trends were calculated. Detailed descriptions of all variables are provided in Supplementary Table 1.

We developed Random Forest (RF) models using these factors as predictors. RF, a data-driven machine learning algorithm, is well-suited for analyzing large datasets due to its ability to handle complex relationships without requiring statistical assumptions about predictors or target variables[63]. To interpret RF results, SHAP was used to quantify the marginal contributions of each predictor to the target variable. Variable importance was assessed using absolute SHAP values, calculated as the absolute weighted average of marginal contributions, to rank predictors[64] and identify dominant factors influencing the spatial variability of $N_{deposition}$ effects. The RF models were implemented using the "ranger" package[65], and SHAP values were extracted using the "treeshap" package in R[66].

Exploration of the mediators to link $N_{deposition}$ with DFS

We performed pixel-level partial correlation analyses to examine the intermediary roles of growing-season LAI, SIF, and ET in linking $N_{deposition}$ to DFS, while controlling effects of climatic drivers. Statistical significance was determined at $p < 0.05$. To further explore these relationships, we applied structural equation modeling (SEM) to quantify both direct and indirect causal pathways between $N_{deposition}$ and DFS, accounting for changes in LAI, SIF, and ET. Regions were categorized into two groups based on the correlation between $N_{deposition}$ and satellite-based DFS: (G1) records or pixels with significantly positive correlations and (G2) records or pixels with significantly negative correlations ($p < 0.05$). For each group, we analyzed three key pathways linking $N_{deposition}$ to DFS: foliar expansion (via LAI), increased productivity (via SIF), and accelerated water dynamics (via ET). For in situ-based analyses, before conducting SEM, we determined species-combined average DFS for each site ($n = 46$), and extracted site-level $N_{deposition}$, LAI, SIF, and ET.

All variables were standardized prior to analysis, and path coefficients were estimated using maximum-likelihood estimation. Path effects were computed as the product of standardized coefficients along each pathway, while the total effect of a variable was determined by summing all path effects involving that variable. The validity of the SEM was assessed using standard fit criteria: the χ^2 test ($p > 0.05$), comparative fit index (CFI > 0.9), standardized root mean square residual (SRMR < 0.08), goodness of fit index (GFI > 0.95), and root mean square error of approximation (RMSEA < 0.08). A model was considered valid if it met at least three of these five criteria[67]. SEMs were constructed and analyzed using the "lavaan" package in R[68].

Reporting summary

Further information on research design is available in the Nature Portfolio Reporting Summary linked to this article.

Data availability

All data used in this study are freely available from the following sources: In situ DFS data are provided by the China Phenological Observation Network (CPON, http://www.cpon.ac.cn/). GIMMS NDVI is available from https://daac.ornl.gov/cgi-bin/dsviewer.pl?ds_id=2187. MODIS NDVI is available from https://lpdaac.usgs.gov/products/mod13c2v061/. SIF is available from https://zenodo.org/records/14586458. Ku-band VOD is available from https://zenodo.org/records/2575599. GIMMS LAI is available from https://zenodo.org/records/8281930. CN05.1 monthly climatic data is available from https://ccrc.iap.ac.cn/resource/detail?id=228. Plant N uptake, N use efficiency, N resorption efficiency are available from https://doi.org/10.5281/zenodo.8182205. GLEAM data is available from https://www.gleam.eu/. Species richness is available from https://science-i.org/gfb2-co-limitation/. Tree density is available from https://elischolar.library.yale.edu/yale_fes_data/1/. Forest age is available from https://www.bgc-jena.mpg.de/geodb/projects/FileDetails.php. Above- and below-ground biomass are available from https://zenodo.org/records/13331493. Maximum root depth is available from https://wci.earth2observe.eu/thredds/catalog/usc/root-depth/catalog.html. SoilGrids 2.0 data is available from https://files.isric.org/soilgrids/latest/. CLCD data is available from https://doi.org/10.5281/zenodo.4417810. Field measurements of $N_{deposition}$ are available from https://doi.org/10.6084/m9.figshare.26778574. Source data are provided with this paper.

Code availability

All data analyses and modeling were performed using R (v4.3.1) or Python (v3.12). The code is stored in a publicly available Zenodo repository https://zenodo.org/records/14588235.

References

1. Liu, X. et al. Enhanced nitrogen deposition over China. *Nature* **494**, 459–462 (2013).
2. Yu, G. et al. Stabilization of atmospheric nitrogen deposition in China over the past decade. *Nat. Geosci.* **12**, 424–429 (2019).
3. Ackerman, D., Millet, D. B. & Chen, X. Global estimates of inorganic nitrogen deposition across four decades. *Glob. Biogeochem. Cycles* **33**, 100–107 (2019).
4. Reay, D. S. et al. Global nitrogen deposition and carbon sinks. *Nat. Geosci.* **1**, 430–437 (2008).
5. Liu, X. et al. Nitrogen deposition and its ecological impact in China: an overview. *Environ. Poll.* **159**, 2251–2264 (2011).
6. Peñuelas, J. et al. Human-induced nitrogen–phosphorus imbalances alter natural and managed ecosystems across the globe. *Nat. Commun.* **4**, 2934 (2013).
7. Maskell, L. C. et al. Nitrogen deposition causes widespread loss of species richness in British habitats. *Glob. Change Biol.* **16**, 671–679 (2010).
8. Nacry, P., Bouguyon, E. & Gojon, A. Nitrogen acquisition by roots: physiological and developmental mechanisms ensuring plant adaptation to a fluctuating resource. *Plant Soil* **370**, 1–29 (2013).
9. Masclaux-Daubresse, C. et al. Nitrogen uptake, assimilation and remobilization in plants: challenges for sustainable and productive agriculture. *Ann. Bot.* **105**, 1141–1157 (2010).
10. Liu, M. et al. Nitrogen availability in soil controls uptake of different nitrogen forms by plants. *N. Phytol.* **245**, 1450–1467 (2025).
11. Keskitalo, J. et al. A cellular timetable of autumn senescence. *Plant Physiol.* **139**, 1635–1648 (2005).
12. Fu, Y. H. et al. Nutrient availability alters the correlation between spring leaf-out and autumn leaf senescence dates. *Tree Physiol.* **39**, 1277–1284 (2019).
13. Wingler, A. et al. The role of sugars in integrating environmental signals during the regulation of leaf senescence. *J. Exp. Bot.* **57**, 391–399 (2006).
14. Richardson, A. D. et al. Climate change, phenology, and phenological control of vegetation feedbacks to the climate system. *Agric. Forest Meteorol.* **169**, 156–173 (2013).
15. Wu, C. et al. Interannual variability of net ecosystem productivity in forests is explained by carbon flux phenology in autumn. *Glob. Ecol. Biogeogr.* **22**, 994–1006 (2013).
16. Keenan, T. F. et al. Net carbon uptake has increased through warming-induced changes in temperate forest phenology. *Nat. Clim. Change* **4**, 598–604 (2014).
17. Garonna, I. et al. Strong contribution of autumn phenology to changes in satellite-derived growing season length estimates across Europe (1982–2011). *Glob. Change Biol.* **20**, 3457–3470 (2014).
18. Richardson, A. D. et al. Terrestrial biosphere models need better representation of vegetation phenology: results from the North American carbon program site synthesis. *Glob. Change Biol.* **18**, 566–584 (2012).
19. Lagercrantz, U. L. F. At the end of the day: a common molecular mechanism for photoperiod responses in plants? *J. Exp. Bot.* **60**, 2501–2515 (2009).
20. Welling, A. & Palva, E. T. Molecular control of cold acclimation in trees. *Physiologia. Plantarum.* **127**, 167–181 (2006).

21. Piao, S. et al. Plant phenology and global climate change: current progresses and challenges. *Glob. Change Biol.* **25**, 1922–1940 (2019).
22. Wu, C. et al. Widespread decline in winds delayed autumn foliar senescence over high latitudes. *Proceed. Natl Acad. Sci. USA* **118**, e2015821118 (2021).
23. Vitasse, Y. et al. Responses of canopy duration to temperature changes in four temperate tree species: relative contributions of spring and autumn leaf phenology. *Oecologia* **161**, 187–198 (2009).
24. Wang, P. et al. Delayed autumnal leaf senescence following nutrient fertilization results in altered nitrogen resorption. *Tree Physiol.* **42**, 1549–1559 (2022).
25. Wang, C. & Tang, Y. Responses of plant phenology to nitrogen addition: a meta-analysis. *Oikos* **128**, 1243–1253 (2019).
26. Cleland, E. E. et al. Diverse responses of phenology to global changes in a grassland ecosystem. *Proc. Natl Acad. Sci.* **103**, 13740–13744 (2006).
27. Vitasse, Y. et al. Impact of microclimatic conditions and resource availability on spring and autumn phenology of temperate tree seedlings. *N. Phytol.* **232**, 537–550 (2021).
28. Niinemets, Ü. & Tamm, Ü. Species differences in timing of leaf fall and foliage chemistry modify nutrient resorption efficiency in deciduous temperate forest stands. *Tree physiol.* **25**, 1001–1014 (2005).
29. Schippers, J. H. et al. Living to die and dying to live: the survival strategy behind leaf senescence. *Plant Physiol.* **169**, 914–930 (2015).
30. Estiarte, M. & Peñuelas, J. Alteration of the phenology of leaf senescence and fall in winter deciduous species by climate change: effects on nutrient proficiency. *Glob. Change Biol.* **21**, 1005–1017 (2015).
31. Zani, D. et al. Increased growing-season productivity drives earlier autumn leaf senescence in temperate trees. *Science* **370**, 1066–1071 (2020).
32. Zhang, Y. J. et al. Extended leaf senescence promotes carbon gain and nutrient resorption: importance of maintaining winter photosynthesis in subtropical forests. *Oecologia* **173**, 721–730 (2013).
33. Aerts, R. Nutrient resorption from senescing leaves of perennials: are there general patterns? *J. Ecol.* **84**, 597–608 (1996).
34. Sanczuk, P. et al. Unexpected westward range shifts in European forest plants link to nitrogen deposition. *Science* **386**, 193–198 (2024).
35. Lu, X. & Keenan, T. F. No evidence for a negative effect of growing season photosynthesis on leaf senescence timing. *Glob. Change Biol.* **28**, 3083–3093 (2022).
36. Norby, R. J. Comment on "Increased growing-season productivity drives earlier autumn leaf senescence in temperate trees. *Science* **371**, eabg1438 (2021).
37. Taylor, G. et al. Future atmospheric CO2 leads to delayed autumnal senescence. *Glob. Change Biol.* **14**, 264–275 (2008).
38. Norby, R. J. et al. CO_2 enhancement of forest productivity constrained by limited nitrogen availability. *Proc. Natl Acad. Sci. USA* **107**, 19368–19373 (2010).
39. Wu, C. et al. Increased drought effects on the phenology of autumn leaf senescence. *Nat. Clim. Change* **12**, 943–949 (2022).
40. Ge, Q. et al. Phenological response to climate change in China: a meta-analysis. *Glob. Change Biol.* **21**, 265–274 (2015).
41. Wang, J. et al. Decreasing rainfall frequency contributes to earlier leaf onset in northern ecosystems. *Nat. Clim. Change* **12**, 386–392 (2022).
42. Shen, M. et al. Can changes in autumn phenology facilitate earlier green-up date of northern vegetation? *Agric. Forest Meteoro.* **291**, 108077 (2020).
43. Chen, J. et al. A simple method for reconstructing a high-quality NDVI time-series data set based on the Savitzky–Golay filter. *Remote Sens. Environ.* **91**, 332–344 (2004).
44. White, M. A., Thornton, P. E. & Running, S. W. A continental phenology model for monitoring vegetation responses to interannual climatic variability. *Glob. Biogeochem. Cycles* **11**, 217–234 (1997).
45. Gu, F. et al. Nitrogen deposition and its effect on carbon storage in Chinese forests during 1981–2010. *Atmos. Environ.* **123**, 171–179 (2015).
46. Zhu, J. et al. Changing patterns of global nitrogen deposition driven by socio-economic development. *Nat. Commun.s* **16**, 46 (2025).
47. Wu, J. et al. Changes of effective temperature and cold/hot days in late decades over China based on a high resolution gridded observation dataset. *Int. J. Climatol.* **37**, 788–800 (2017).
48. Yang, J. & Huang, X. The 30 m annual land cover dataset and its dynamics in China from 1990 to 2019. *Earth Syst. Sci. Data* **13**, 3907–3925 (2021).
49. Peng, Y. et al. Global terrestrial nitrogen uptake and nitrogen use efficiency. *J. Ecol.* **111**, 2676–2693 (2023).
50. Mo, L. et al. The global distribution and drivers of wood density and their impact on forest carbon stocks. *Nat. Ecol. Evol.* **8**, 2195–2212 (2024)
51. Liang, J. et al. Co-limitation towards lower latitudes shapes global forest diversity gradients. *Nat. Ecol. Evo.* **6**, 1423–1437 (2022).
52. Simon, B. et al. Mapping global forest age from forest inventories, biomass and climate data. *Earth Syst.Sci. Data* **13**, 4881–4896 (2021).
53. Crowther, T. W. et al. Mapping tree density at a global scale. *Nature* **525**, 201–205 (2015).
54. Fan, Y. et al. Hydrologic regulation of plant rooting depth. *Proc. Natl Acad. Sci. USA* **114**, 10572–10577 (2017).
55. Poggio, L. et al. SoilGrids 2.0: producing soil information for the globe with quantified spatial uncertainty. *Soil* **7**, 217–240 (2021).
56. Moesinger, L. et al. The global long-term microwave vegetation optical depth climate archive (VODCA). *Earth Syst. Sci. Data* **12**, 177–196 (2020).
57. Cao, S. et al. Spatiotemporally consistent global dataset of the GIMMS leaf area index (GIMMS LAI4g) from 1982 to 2020. *Earth Syst. Sci. Data* **15**, 4877–4899 (2023).
58. Lian, X. et al. Diminishing carryover benefits of earlier spring vegetation growth. *Nat. Ecol. Evol.* **8**, 218–228 (2024).
59. Miralles, D. G. et al. Global land-surface evaporation estimated from satellite-based observations. *Hydrol. Earth Syst. Sci.* **15**, 453–469 (2011).
60. Spirtes, P. & Glymour, C. An algorithm for fast recovery of sparse causal graphs. *Soc. Sci. Comput. Rev.* **9**, 62–72 (1991).
61. Runge, J. et al. Inferring causation from time series in earth system sciences. *Nat. Commun.* **10**, 1–13 (2019).
62. Runge, J. Discovering contemporaneous and lagged causal relations in autocorrelated nonlinear time series data sets. In *Conference on uncertainty in artificial intelligence*, 1388–1397 (PMLR, 2020).
63. Breiman, L. Random forests. *Mach. Learn.* **45**, 5–32 (2001).
64. Berdugo, M. et al. Prevalence and drivers of abrupt vegetation shifts in global drylands. *Proc. Natl Acad. Sci. USA* **119**, e2123393119 (2022).
65. Wright, M. N. & Ziegler, A. Ranger: a fast implementation of random forests for high dimensional data in C++ and R. *J. Stat. Softw.* **77**, 1–17 (2017).
66. Lundberg, S. M., Erion, G. G. & Lee, S.-I. Consistent individualized feature attribution for tree ensembles. *arXiv* https://doi.org/10.48550/ARXIV.1802.03888. (2018).
67. Gao, S. et al. An earlier start of the thermal growing season enhances tree growth in cold humid areas but not in dry areas. *Nat. Ecol. Evol.* **6**, 397–404 (2022).
68. Rosseel, Y. Lavaan: an R package for structural equation modeling. *J. Stat. Softw.* **48**, 1–36 (2012)

Acknowledgements
This study was supported by National Natural Science Foundation of China grant (42125101). J.W. was funded by the "Kezhen and Bingwei" Young Scientist Program of IGSNRR. X.W. was funded by the National Natural Science Foundation of China (42271034) and Youth Innovation Promotion Association of Chinese Academy of Sciences (2022051). J.P. was supported by the Spanish Government grants TED2021-132627 B–I00 and PID2022-140808NB-I00, funded by MCIN, AEI/10.13039/501100011033 European Union Next Generation EU/PRTR, and the Fundación Ramón Areces grant CIVP20A6621.

Author contributions
C.W. designed the research. J.W. and X.W. wrote the first draft of the manuscript. J.W. performed the analyses and visualization. X.W. and H.H. calculated satellite-based phenology datasets. J.P. discussed the design, methods and results and substantially revised the manuscript with intensive suggestions.

Competing interests
The authors declare no competing interests.

Additional information
Supplementary information The online version contains supplementary material available at https://doi.org/10.1038/s41467-025-59000-0.

Correspondence and requests for materials should be addressed to Chaoyang Wu.

Peer review information *Nature Communications* thanks Line Nybakken, Helena Vallicrosa and the other, anonymous, reviewer(s) for their contribution to the peer review of this work. A peer review file is available.